Communications Earth & Environment https://doi.org/10.1038/s43247-026-03296-3

Article in Press

A deformation-driven earthquake interaction model for seismicity at Campi Flegrei

Received: 15 August 2025

Accepted: 3 February 2026

Cite this article as: Hainzl, S., Dahm, T., Tramelli, A. A deformation-driven earthquake interaction model for seismicity at Campi Flegrei. *Commun Earth Environ* (2026). https://doi.org/10.1038/s43247-026-03296-3

Sebastian Hainzl, Torsten Dahm & Anna Tramelli

A deformation-driven earthquake interaction model for seismicity at Campi Flegrei

Introduction

The Campi Flegrei caldera in Italy (Fig. 1a) has a complex magma plumbing system consisting of various reservoir levels in the crust and upper mantle. Magmatic and hydrothermal processes lead to deformation cycles that are often associated with intense earthquake activity . Occasionally, these cycles end in volcanic eruptions that form new maars or cones . The last eruption occurred at Monte Nuovo in 1538, following a short period of lateral magma propagation, which was preceded by a long uplift period from 1400 to 1536 related to a source consistent with the source of the present-day uplift, as determined by geodetic data . Since 2005, the caldera has experienced accelerated uplift of over one meter, accompanied by a strong increase in shallow earthquakes, prompting concerns about potential future volcanic unrest and associated seismic hazards in the metropolitan area of Naples. This ongoing uplift period is part of a long period of ground deformation involving inflation and deflation, including three additional uplift periods in the last century, notably in 1950–52, 1969–72, and 1982–84 (see Fig. 1b). During these periods, rapid ground uplift and increased seismic activity (bradyseisms) partly prompted emergency responses and temporary evacuations .

The uplift and seismicity in Campi Flegrei are attributed to the pressurization of a gas-rich reservoir at 3-4 km depth rather than the result of direct magmatic intrusion . Since 1905, seismicity has mainly occurred during uplift periods, with local seismicity recorded in the national HORUS catalog during the last two uplift episodes (Fig. 1b). During the preceding uplift period between 1969 and 1972, about 2,600 local earthquakes were also recorded, although magnitudes were not calculated . However, the earthquake rate is not simply proportional to the uplift rate. Instead, it exhibits a nonlinear relationship with ground uplift, characterized by an increasing ratio between earthquake rate and uplift rate, as recently demonstrated by Tramelli et al. .

A nonlinear seismicity response can be explained by delayed triggering due to rate-and-state-dependent friction known from laboratory rock experiments. Specifically, the Rate-and-State (RS) seismicity model predicts delayed onsets and nonlinear responses to stress changes. For example, the RS model and its generalization have been used to explain the delayed onset and acceleration of seismicity observed in the Groningen gas field in the Netherlands, which is related to gas extraction . Beyond the uplift-related long-term trends, the seismicity in Campi Flegrei is characterized by temporal clustering, manifesting as earthquake swarms rather than mainshock–aftershock sequences. Such swarm-like behavior is frequently observed in other volcanic and hydrothermal regions, such as NW Bohemia in central Europe, where episodic magmatic fluid intrusions, primarily composed of CO_2, are known to trigger clustered seismic activity resulting from complex fluid-earthquake interactions, including aftershocks . The statistical standard model for short-term clustering is the Epidemic-Type Aftershock Sequence (ETAS) model . In this study, we test a hybrid approach combining the RS model with ETAS , aiming to simultaneously capture both the physics of stress-driven changes and the statistical features of earthquake clustering.

We demonstrate that the general seismicity evolution observed over the last hundred years can be explained by stress shadowing and loading when considering the statistical response of frictional faults, while earthquake interactions effectively capture clustering patterns. Together, these mechanisms reproduce the seismicity observed in Campi Flegrei and enable probabilistic short-term forecasts of both earthquake rate and maximum magnitude.

Results

Stress shadowing and Kaiser effect

Our analysis relies on earthquake catalog and deformation data, where the latter consists of the long-term level data since 1905, taken from Del Gaudio et al. , and the short-term data from the co-located GPS station RITE. For the seismicity data since 2005, we use the local catalog with duration magnitudes provided by the Observatorio Vesuviano with a cutoff magnitude (M_c) of 0.45, based on our estimate of the completeness magnitude described in the Methods section. For the analysis of the seismicity at Campi Flegrei on a longer time scale, we use the HORUS catalog with homogenized moment magnitudes for earthquakes in Italy since 1960 , selecting events with distances less than 20 km from the RITE GPS station (yellow triangle in Fig. 1a). For the latter, we choose a conservative cutoff magnitude of M_C = 3.0 based on the analysis presented in the Methods section. A recently published catalog for Campi Flegrei based on a machine learning approach includes over 50,000 earthquakes from 2022 to 2025 , providing high-quality locations that delineate the area affected by the current uplift-induced seismicity. However, the catalog is not useful for this study due to its short temporal coverage and the use of relative rather than absolute magnitudes.

The time series of observed uplift and seismicity is shown in Fig. 1(b,c). Between 1905 and 1950, the Campi Flegrei gradually subsided by more than 1 m. Uplift episodes occurred between 1950-52, 1969-72, 1982-84, and since 2004. The first reported seismicity occurred in 1970, when the uplift exceeded the initial value for the first time. At that time, a newly installed seismic network of three seismometers registered about 2,600 events between 28 February 1970 and 30 October 1971, but no magnitudes were attributed to them . The first events in the HORUS catalog were recorded in 1983, when the uplift exceeded its previous peak from 1972. Then, their occurrence stopped when the surface started to subside after reaching its new peak value in early 1985. According to the HORUS catalog, subsequent earthquakes with $M_W \geq 3$ occurred only after the uplift in 2022 surpassed its earlier peak. Thus, in all cases, the main activity occurred after the uplift had exceeded its previous maximum. This observation agrees with the well-known Kaiser effect , namely the phenomenon in materials science and rock mechanics that a material subjected to cyclic loading does not emit acoustic emissions until the previously applied maximum stress level is exceeded. In seismology, the Kaiser effect is not as well-known as stress shadowing, which describes the temporary inhibition of seismicity in an area where stress is reduced. Unlike the Kaiser effect, however, stress shadowing does not specify when reactivation will occur.

However, despite the general agreement, the Kaiser effect can not explain the details. The uplift period since 2005 shows that there is a continuous acceleration of $M_d \geq 0.45$ events in the local catalog before and after the prior uplift maximum was exceeded in early 2022, rather than a sharp onset (Figure 1c). It is likely that catalog incompleteness, i.e., the high magnitude threshold, masks a similarly gradual onset and decay of seismic activity during earlier uplift episodes.

Aftershock triggering

While the long-term trend of earthquake occurrence is related to uplift, seismic activity clusters strongly on short time scales, which is not related to observed deformation (Fig. 1c). Earthquake clustering is a well-known phenomenon for natural seismicity, often associated with mainshock-aftershock sequences, where the co- and postseismic stress changes due to the mainshock trigger aftershocks. The rate of aftershocks is well described by the Omori-Utsu law, which expresses the aftershock rate R as a function of time t after the mainshock by

$$R(t,m) = K(m)(c+t)^{-p}$$

with c being a small delay time and $p \approx 1$. The number of aftershocks is found to depend exponentially on the mainshock magnitude, $K(m) \sim 10^{\alpha m}$.

At first glance, the observed clusters appear swarm-like, with no dominant mainshocks, see an example shown in the left inset of Fig. 2a. However, mainshock-aftershock patterns can be obscured by overlapping activity. To determine whether aftershocks are present, we stack the recorded earthquakes relative to the times of the largest events. If the occurrence

of the large events does not influence the activity, the activity before and after those events should be similar. In contrast, if aftershocks are triggered, the earthquake occurrence directly after the large events should be elevated relative to the preceding time. Figure 2(a) shows the stack of the recorded $M_d > 0.45$ events within plus and minus half a day relative to the occurrence times of the 50 earthquakes with $M_d \geq 3$, excluding the latter. The stacked number of earthquakes after the large shocks clearly exceeds the number of events preceding the main events, where the rate of the aftershocks is shown to decay according to the Omori-Utsu law with $p = 0.5$, indicating aftershock triggering. Note that the observed inverse Omori-Utsu law for the foreshocks (blue line in Fig. 2a) can also be explained by aftershock triggering, namely by Omori-Utsu-type aftershocks triggered by events in the preceding period . Aftershock triggering becomes even more evident when we analyze the excess of aftershocks as a function of the mainshock size. Here we simply count the numbers N_1 and N_2 of earthquakes preceding and following an event above a given cutoff magnitude M_c, within a half-day period. Figure 2(b) shows the average difference $\square N_2 - N_1 \square$ for all selected main events as a function of M_c. The same plot also shows the excess of aftershocks over foreshocks for mainshocks in non-overlapping mainshock magnitude bins [1, 2], [2, 3], [3, 4], and [4, 5]. The number of triggered events increases exponentially with mainshock magnitude, in agreement with observations for typical aftershock triggering , with an exponent of $\alpha = 0.5$. In contrast, repeating the analysis for sequences with the observed occurrence times but with randomly reshuffled magnitudes shows no increase (see inset of Fig. 2b), clearly indicating the significance of earthquake-earthquake interactions within the swarm-like clusters.

Deformation-driven modeling of seismicity

A frequently used physics-based seismicity model, which accounts for stress shadowing and loading effects, is the rate-and-state (RS) model introduced by Dieterich . This model assumes that the dynamics of single faults are described by the rate and slip dependence of the frictional strength and the time-dependent restrengthening observed in laboratory experiments. Considering the statistical response of a population of frictional instabilities following the lab-derived constitutive friction law, RS explains many aspects of observed earthquake phenomena, including earthquake clustering and seismic quiescence . It has also been applied to volcanic seismicity and fluid injection and extraction . Assuming an initially critical stress state, the model rate is computed using Eq. ([eq:RS]), which depends on three parameters: the background rate r, the stress sensitivity parameter $A\sigma'$, and the relaxation time t_a. Details of the implementation are provided in the Methods section.

Figure 3(a) shows the fit of the RS model to the $M_d \geq 0.45$ events since 2005, using the maximum likelihood parameters provided in Table 1. In Fig. 3b, the same monthly rates are shown in logarithmic scale to improve the visibility of low rates. While the nonlinear increase in the seismicity is well reproduced, the short-term clustering cannot be explained by the stresses estimated from the uplift data. 22.9% of the observations fall outside the 95% confidence interval of the RS model (blue curves in Fig. 3b), which is calculated by Poisson distribution with a mean equal to the monthly integral of the RS model. The result indicates that the deformation alone is unable to reproduce the swarm-type clustering of the seismicity characterized by aftershock triggering.

Therefore, we use the epidemic-type aftershock sequence (ETAS) model, described in the Methods section, which is the standard model for short-term clustering. This model describes the total earthquake rate as the sum of a background rate μ and the rates of ongoing Omori-type aftershock sequences from previous earthquakes . In this model, the earthquake-earthquake interactions involves the four parameters, K, α, c, and p related to the Omori-Utsu law (Eq. [eq:OU]), where the first two parameters (K, α) represent the exponential scaling of the aftershock productivity as a function of the earthquake magnitude, while c and p refer to the temporal aftershock decay. While the basic ETAS model assumes a constant background rate, the background rate is expected to be time-dependent in the case of transient driving mechanisms , such as those at Campi Flegrei. Therefore, we use the ETAS model with a time-dependent background rate given by the deformation-driven RS model, as explained in the Methods section. This hybrid ETAS model consists of seven parameters, namely $r, A\sigma, t_a, K, \alpha, c$, and p.

Figure 3(a,b) also shows the fit of the hybrid ETAS model based on the maximum likelihood parameters provided in Table 1. The vast majority of the observations fall within

the confidence interval of the hybrid ETAS model, which is calculated by Poisson distribution with a mean equal to the monthly integral of Eq. ([eq:ETAS]). In particular, only 3.3% of the observations fall outside the 95% confidence interval, which is close to the theoretical value of 5% for an infinite sample of observations.

The values of the maximum likelihood parameters of the RS and hybrid ETAS models for the observed $M_d \geq 0.45$ events since 2005 (Table 1) show that the $A\sigma$ parameter is similar for the RS and hybrid ETAS models, while the other two parameters differ significantly. Notably, the RS-only fit yields an overly long relaxation time of $1.5 \cdot 10^6$ years, whereas the hybrid ETAS model yields a more realistic value of $t_a = 34.2$ years. As shown in Supplementary Fig. S3b, increasing t_a strengthens the memory effect, making the RS response progressively more similar to the Kaiser effect. However, the results for $t > 2005$ are almost identical for all t_a-values larger than 50 years, leading to a largely unconstrained t_a-value in the RS-only model. Regarding the ETAS trigger kernel, the hybrid model yields a small α value of 0.24 and a p-value larger than 1, though not constrained to $p > 1$. While a small α value is typical for swarm activity , both values differ significantly from the stacked results presented in Fig. 2. This discrepancy likely arises because the stacked result reflects the dressed decay, i.e., the total activity including background events, the direct aftershocks triggered by the mainshock, and secondary activity triggered by foreshocks or aftershocks, whereas ETAS parameters (K, α, c, p) only describe the bare (direct) aftershocks.

The hybrid ETAS model can also be used to analyze the expected seismicity since 1905. Figure 3(c) shows the results for the period since 1940, using 10,000 Monte Carlo simulations of the hybrid ETAS model with parameters listed in Table 1 and randomly selected magnitudes from the Gutenberg-Richter law with $b = 0.9$ in the range [0.45, 5.0]. The curve and shaded area refer to the mean and 95% confidence interval of the yearly rates, respectively. The model results are compared with the event rates in the HORUS catalog, showing a good agreement with the activity since 1980. In particular, it reproduces the timing of the events in the 1982-1985 period well, with a rather rapid onset and decay of the seismicity. The model predicts no recognizable seismicity for the first uplift period in 1950-1952, which occurred before the beginning of the HORUS catalog in 1960. However, the model predicts earthquakes for the second uplift period in 1969-1972, during which approximately 2,600 events were recorded . Unfortunately, the seismicity rate related to a given magnitude level is unclear for this episode, because no magnitudes were attributed to those events.

Overall, the analysis with parameters optimized for the period [2005, 2025] demonstrates the consistency of hybrid ETAS model with the observations on long and short timescales.

Pseudo-prospective forecast test

We perform a pseudo-prospective test to analyze the model's ability to forecast the seismicity in the next ΔT days based solely on previous observational data. Specifically, we test forecasts of the event number (N) and maximum magnitude (M_{max}) of events with $M_d \geq 0.45$ events in the next week or month. Beginning from 2020, we calculate forecasts starting at T_s with weekly stepping, using 1000 Monte Carlo simulations of the hybrid ETAS model for each forecast. These simulations are based on the model parameters that maximize the likelihood function for the $M_d \geq 0.45$ earthquakes in the period $2005 < t < T_s$, which are illustrated in the Supplementary Fig. S6. In these simulations, the magnitudes are randomly sampled from a doubly truncated Gutenberg-Richter distribution between 0.45 and 5.0, using the maximum likelihood b-value estimated from the preceding events since 2005. The b-values slightly decay from values around 1.0 in the year 2020 to 0.89 for the final value. Furthermore, the forecasts rely on uplift data linearly extrapolated from the last 100 days into the forecast period $[T_s, T_s+\Delta T]$. For each simulation, we store the simulated number of events and the maximum magnitude within the given forecast period. Finally, we evaluate the distribution of the 1000 values of the forward simulations in terms of the mean value and the 68%, 90%, and 95% confidence intervals.

Figure 4 shows the results of this pseudo-prospective test. Panels (a) and (c) show the N and M_{max} forecasts for $\Delta T = 7$ days, and panels (b) and (d) show the corresponding forecasts for $\Delta T = 30$ days. All forecast periods are disjunct for $\Delta T = 7$ days because of

the weekly stepping of the forecast starting time. In contrast, the observations are correlated for ΔT = 30 days because of the overlap between subsequent forecast periods. The test results show promising probabilistic predictions of the hybrid ETAS model. The vast majority of forecasts align with the observations in the sense that the observations fall within the confidence intervals resulting from the aleatoric variability of the model.

After our analyzed data set ended, a magnitude 4.6 event occurred on June 30, 2025. We run forecasts with linearly extrapolated uplift data from the end of the catalog on February 4, 2025, for the next 5 months and 1 year. The forecasts yield an exceedance probability for an M4.6 event of 6.5% and 12.6%, respectively. Therefore, the observed large magnitude is still inside the confidence interval of the model, although on the upper end.

Discussion

The long-term seismicity trend can be modeled by the Rate-and-State (RS) framework, emulating the timing behavior predicted by the Kaiser effect, but predicting a mild initiation and an escalation of activity aligning with the observed trends. Although the RS model imitates the timing patterns of the Kaiser effect by integrating stress history, its friction mechanism differs from classical, damage-based interpretations of the Kaiser effect . To highlight the memory effects in the RS model and its relation to the Kaiser effect, we compare the results using uplift history since 1905 with those based only on the uplift since 2005. The results are shown in the Supplementary Fig. S3, demonstrating that preceding uplift episodes lead to a delayed onset of seismicity in the current uplift period. Furthermore, increasing t_a values strengthens the memory effect and makes the RS response progressively more similar to the Kaiser effect (Supplementary Fig. S3b).

In addition to the long-term trend, the seismicity in Campi Flegrei is also strongly influenced by short-term earthquake clustering, which is well captured by the ETAS model. We show that a hybrid approach - combining the RS model for the non-stationary background rate with ETAS for earthquake–earthquake interactions - reproduces the observations and has predictive capability. For comparison, we also tested simpler models: (i) a linear Coulomb-Failure (CF) model with an earthquake rate proportional to uplift rate, (ii) a standard ETAS model with constant background rate, and (iii) a hybrid CF+ETAS model (see Supplementary Material for details). The CF model fails to reproduce the data, while ETAS and CF+ETAS provide comparable fits to the seismicity since 2005, though both perform slightly worse in terms of AIC and information gain (Supplementary Table S1; Figs. S4, S5a–b). However, neither ETAS nor CF+ETAS captures the century-scale trend (Figs. S4c, S5c), as they lack a physically consistent transient background rate.

The observed swarm-type earthquake clustering likely involve episodic fluid intrusions that are not reflected in the uplift signal. In particular, magmatic fluid intrusion, modulated by the shallow hydrothermal system and its possible permeability variations, is assumed to justify the H_2S increased presence in the fumarole gas composition of the Solfatara . Such fluid signals are not explicitly captured by the hybrid ETAS model, whose background rate only relates to uplift. However, a major part of the clusters is shown to be related to earthquake–earthquake interactions, documented by the Omori-type aftershock triggering and a magnitude scaling of the aftershock numbers. The underlying mechanism can be related to processes such as coseismic stress changes, afterslip, or increased permeability due to preceding earthquakes, enhancing fluid flow . These mechanisms have been well documented in other volcanic regions, such as the Vogtland swarms, where fluid-driven interactions are known to play a critical role in swarm dynamics . While the hybrid ETAS model successfully captures some aspects of clustering, improved modeling of swarm activity in Campi Flegrei would require the inclusion of a time-dependent fluid source term. However, the evolution of such fluid signals is inherently difficult to predict and often becomes, if at all, clear only in retrospect based on geophysical and geochemical observations. Improved modeling would also require accounting for spatial heterogeneities. Different seismic responses due to geological heterogeneity, temperature, and fluid presence are, e.g., evidenced by the *b*-value tomography proposed by .

Taking into account the current unrest, Bevilacqua et al. suggested a squared-exponential increment of the number of earthquakes in time associated with a parabolic increment of the uplift starting in 2020. It was explained by a quasi-elastic and stress-memory behavior of the crust, suggesting a weakening in its mechanical properties. Kilburn et al. also claimed an inelastic deformation regime of the Campi Flegrei shallow crust since 2020. In

contrast, our model explains the nonlinear seismicity response solely by frictional fault responses based on a linear stress-strain relation. However, in the later phases, particularly since late 2023, uplift is associated with a stronger and more frequent swarm response. This increased swarm activity is possibly amplified by unseen or transient fluid effects and extensified aftershock triggering expressed by a rising branching ratio within the ETAS framework (see Supplementary Fig. S6). The increased branching ratio with time indicates a higher degree of earthquake clustering and secondary triggering, although this trend may be partly affected by variations in sample size .

However, it is important to emphasize that our modeling approach assumes a stationary pressure source drives the observed uplift at the RITE site. Under this assumption, Coulomb stress within the crustal volume can be considered proportional to uplift at this location by a constant proportionality factor. However, if the pressure source begins to migrate, this relationship between Coulomb stress changes and uplift at the RITE station will change, requiring a new model calibration. Such a scenario happened before the last eruption in 1538, when the same stationary source first led to a long uplift period before a lateral transfer of magma fed the non-central eruption at Monte Nuovo .

In summary, this study demonstrates that the seismicity in Campi Flegrei is closely linked to ground uplift, with a notably nonlinear and accelerating response since 2005. While the Kaiser effect explains major parts of the seismicity response due to uplift in the last 100 years, it fails to explain it in detail. In contrast, we show that the Rate-and-State (RS) model captures the long-term evolution of seismicity by accounting for delayed triggering resulting from time-dependent stress loading. Additionally, the observed short-term clustering of earthquakes is found to include embedded aftershock sequences, which can be effectively modeled using the ETAS framework. By combining RS and ETAS models, we show that the observed seismicity patterns can be reproduced. This hybrid model also provides reasonable probabilistic short-term forecasts of earthquake rates and magnitudes.

Overall, the hybrid modeling approach is a promising tool for improving seismic hazard assessments in the Campi Flegrei area, facilitating both probabilistic short-term forecasts and medium-term scenario simulations. This approach may also be relevant for other volcanic systems.

Methods

Estimation of the completeness magnitude

The cutoff magnitudes M_c for the local and the HORUS catalogs are chosen based on fits of the empirical magnitude distribution by the model of Ogata and Katsura , which assumes that the true frequency of events with magnitude m is given by the Gutenberg-Richter distribution, $N(m) \propto b10^{-bm}$. The observable distribution results from the multiplication of this distribution by the detection probability, which is expressed by a cumulative normal distribution with mean μ and standard deviation σ. The model is found to fit the empirical distribution of the local catalog well with the maximum likelihood parameters $b = 0.91, \mu = -0.05$, and $\sigma = 0.42$, see Supplementary Fig. S1. According to these values, the detection probability of an event with magnitude $M_c = 0.45$ is about 90% for earthquakes since 2005.

A corresponding analysis has been performed for the regional events included in the HORUS catalog with homogenized magnitudes for earthquakes in Italy since 1960 . First, we selected the events with distances less than 20 km from the RITE GPS station (yellow triangle in Fig. 1a). The resulting maximum likelihood parameters are $b = 0.76 \pm 0.02, \mu = 1.06 \pm 0.02$, and $\sigma = 0.27 \pm 0.01$. The result is shown in the Supplementary Fig. S2(a), indicating a completeness magnitude of about 1.5. However, the fit is not good, and the completeness magnitude changed over time because of improvements in the seismic network, which is overprinted by the fact that the large majority of events occurred after 2000. To focus on earlier events, we selected events before 1990, but increased the search radius to 100 km to increase the number of events sufficiently to allow a statistical analysis. The fit to these events is shown in panel (b) of the Supplementary Fig. S2, showing a good model fit with maximum likelihood parameters $b = 0.68 \pm 0.03, \mu = 2.19 \pm 0.04$, and $\sigma = 0.35 \pm 0.02$. Based on this result, we chose a conservative cutoff

magnitude of M_c = 2.95 for the HORUS events, corresponding to a detection probability of about 99% for the smallest events.

Rate-State (RS) seismicity model

A prominent physics-based seismicity model, which can account for stress shadowing and loading, is the rate-and-state (RS) model introduced by Dieterich . This model assumes that the dynamics of single faults are described by the rate and slip dependence of the frictional strength and the time-dependent restrengthening observed in laboratory experiments. Considering the statistical response of a fault population with frictional instabilities following the lab-derived constitutive friction law, RS explains many aspects of observed earthquake phenomena, including earthquake clustering and seismic quiescence . It has also been applied to volcanic seismicity and fluid injection and extraction . Lacking information about the initial stress state in 1905, we assume an initially critical stress state with an initially constant reference rate r of $m \geq M_c$ events, which is related to a constant background stressing rate $\dot{\tau}$. Based on this assumption, we can calculate the seismicity rate of the RS model in response to can be calculated for a given time evolution of the Coulomb stress $S(t)$ by

$$\label{eq:RS} R_\mathrm{RS}(t) = r \frac{e^{S(t)/A\sigma}}{1+1/t_\mathrm{a} \int_0^t e^{ S(t')/A\sigma}dt'}$$

with definition $t_a = A\sigma/\dot{\tau}$, which is often called relaxation time or aftershock duration . The model parameter $A\sigma$ is the product of the effective normal stress σ acting on the faults and the dimensionless constitutive friction parameter A, which is usually of the order of 0.01 .

Although it would be more realistic to apply the RS model to stresses computed in the fully specified 3D seismogenic volume of Campi Flegrei with detailed pressure source, fault geometries, and initial stress states, this approach is currently impractical for seismic hazard assessment due to large uncertainties in source processes and missing or incomplete structural and stress information. For simplification, we therefore ignore the spatial component and assume that the stress evolution $S(t)$ is proportional to the uplift $u_z(t)$ at the RITE GPS station. Such a linear correlation, $S(t) = \kappa u_z(t)$, is expected with a spatially stationary pressure source at depth, constant earthquake mechanisms, and a linear elastic crust. In this case, the relative change of all deformation and stress tensor elements are proportional to the relative change of the pressure of the source (p_s), i.e. $S(t)/S_0 = u_z(t)/u_{z,0} = p_s(t)/p_{s,0}$, resulting in $S(t) = \kappa u_z(t)$ with the proportionality factor $\kappa = S_0/u_{z,0}$. Here, we only consider a representative value of S_0, respectively κ, although it may vary depending on the earthquake location and mechanism. Furthermore, because the RS model only depends on the ratio $S(t)/A\sigma = \kappa u_z(t)/A\sigma = u_z(t)/A\sigma'$ with $A\sigma' = A\sigma/\kappa$, we use $u_z(t)$ instead of $S(t)$ in Eq. ([eq:RS]) and estimate the parameter $A\sigma'$, which has units of meters instead of Pascals.

It is important to note that the model rate $R_{RS}(t)$ is always computed using the complete uplift history since 1905, even when fitting or forecasting seismicity for the period after 2005, to account for memory effects of the preceding stress history.

Epidemic-type aftershock sequence (ETAS) model

The standard model for aftershock activity is the epidemic-type aftershock sequence (ETAS) model, describing the total earthquake rate as the sum of a background rate μ and the rates of ongoing Omori-type aftershock sequences from previous earthquakes . The original ETAS model assumes a constant μ, but the background rate is time-dependent in the case of transient driving mechanisms , such as those at Campi Flegrei. The rate of $m \geq M_c$ earthquakes is given in the ETAS model by

$$\label{eq:ETAS} R(t) = \mu(t) + \sum\limits_{i: t_i<t} K\, 10^{\alpha(m_i - M_\mathrm{c})}\, (c+t-t_i)^{-p} H(t_i+T-t)$$

where the index i refers to past events occurring at times t_i with magnitudes $m_i \geq M_c$, assuming that the earthquake catalog is complete for $m \geq M_c$ events . The Heaviside

function, donated as H, assigns a value of 1 for positive arguments and zero otherwise. In the standard ETAS model, the maximum aftershock triggering time, T, is assumed to be infinite. However, according to the RS model, T should be inversely proportional to the stressing rate. For small tectonic deformation rates, T is expected to be in the order of years or decades , but much smaller in Campi Flegrei because of the large deformation rates. Here, we arbitrarily set it to 100 days, but checked that the results do not depend crucially on the choice of this value. The triggering part then involves the four parameters, K, α, c, and p, where the first two parameters (K, α) represent the exponential scaling of the aftershock productivity as a function of the triggering earthquake magnitude, while c and p refer to the well-known Omori-Utsu law for the temporal aftershock decay . In our application, the rate of independent background events $\mu(t)$ is given by the deformation-driven RS model, i.e., $\mu(t) = R_{\mathrm{RS}}(t)$ given by Eq. ([eq:RS]). Thus, the full model consists of seven parameters, namely $r, A\sigma, t_a, K, \alpha, c$, and p.

In general, geodetic measurements include coseismic signals that should be removed before using the RS model for the background seismicity, to minimize the effect of double-counting earthquake-induced stress in the hybrid model. While this is negligible for the moderate-sized earthquakes at Campi Flegrei, it may become important in applications with large earthquakes.

Alternatively to the hybrid model, the RS model could be used alone by explicitly incorporating coseismic stress changes, as the RS model also explains aftershock triggering. For a single coseismic stress step ΔS, the RS model predicts an aftershock decay following the Omori–Utsu law with $p = 1.0, c = t_a \exp(-\Delta S/A\sigma)$, and an exponential roll-off at t_a . However, these analytic relations break down for realistic spatially heterogeneous coseismic stress changes and when the background rate is transient, as at Campi Flegrei. A fully consistent RS approach would require computing all coseismic stress changes on a 3D spatial grid of the Campi Flegrei region, summing both external (fluid-driven) and internal (coseismic) stress contributions, which is infeasible given the limited and uncertain information on slip distributions and focal mechanisms.

Parameter estimation

To estimate the free model parameters, we employ the maximum likelihood method , where the likelihood function L represents the joint probability function for a given model and is constructed by multiplying the probability density functions of all data points. Specifically, the log-likelihood value for the Z earthquakes that occurred at times t_i within the fitting period $[T_0, T_1]$ is calculated using the equation

$$\begin{aligned} \label{eq:LL} \ln{L}(\Theta) &=& \sum_{i=1}^Z \ln{R(t_i|\Theta)} - \int_{T_0}^{T_1} R(t|\Theta)\, dt \ , \end{aligned}$$

where Θ represents the set of fitting parameters . The model parameters are determined by maximizing the $\ln L$ function. We verified that the result represents the global maximum using, in addition, a Bayesian approach described in the Supplementary Material.

To compare the fits of the RS and ETAS models with different numbers (N_f) of free parameters, we utilize the Akaike Information Criterion (AIC), defined as $\mathrm{AIC} = 2(N_f - \ln L)$. A lower AIC value indicates better model performance. Additionally, we calculate the information gain per earthquake (IGPE) of the models relative to the Poisson model, defined as $\mathrm{IGPE} = -(\mathrm{AIC} - \mathrm{AIC}_{\mathrm{Poisson}})/(2Z)$.

Data availability

The local catalog is provided by the Observatorio Vesuviano (https://terremoti.ov.ingv.it/gossip/flegrei), which we accessed on February 26, 2025. The HORUS catalog, which provides homogenized magnitudes for earthquakes in Italy since 1960, can be downloaded at https://horus.bo.ingv.it. The GPS data of the RITE station were extracted from Tramelli et al. and weekly reports compiled by the Observatorio Vesuviano (https://www.ov.ingv.it/index.php/monitoraggio-e-infrastrutture/bollettini-tutti/settimanali-dei-campi-flegrei). We linearly interpolated these data on equidistant time

steps with a step size of seven days between 1905 and February 5, 2025. The Python codes for parameter estimation and forecasting, as well as for reproducing the manuscript figures, can be found at the Zenodo repository (https://doi.org/10.5281/zenodo.18413119).

Acknowledgements

We thank Yuan-Kai Liu and an anonymous reviewer for their constructive and insightful comments, which greatly helped to improve the manuscript. This study has been partly funded by the Deutsche Forschungsgemeinschaft (DFG)- Project-ID 318763901 - SFB1294, project B04. Open access funding provided by GFZ Helmholtz Centre for Geosciences, enabled by Projekt DEAL.

Author contribution

Competing interests

The authors declare no competing interests.

Maximum likelihood model parameters for the fit of the $Z = 4250$ events with $M_d \geq 0.45$ in the period 2005-2025. The hybrid ETAS model has a lower Akaike Information Criterion (AIC) and higher log-likelihood values ($\ln L$) and information gains (IGPE), indicating a superior fit of the hybrid ETAS model. Here, IGPE is calculated relative to the Poisson model. See the Methods section for more details.

Model	r [yr^{-1}]	$A\sigma'$ [m]	t_a [yr]	K	α	c [s]	p	$\ln L$	AIC	IGPE
RS	0.002	0.19	1.5e+06	–	–	–	–	-1229.6	2465.3	1.26
ETAS	7.5	0.20	34.2	0.04	0.24	51.8	1.08	4125.9	-8237.8	2.52

Bradyseims at Campi Flegrei. (a) Map of Campi Flegrei with $M_d \geq 0.45$ earthquakes recorded since 2005 (blue points) . (b, c) Observed uplift (curves) compared to recorded seismicity (points): (b) Long-term uplift history since 1905 (left scale) according to Del Gaudio et al. and the RITE GPS station (yellow triangle in panel (a) with recorded $M_w \geq 3$ events within 20 km in the HORUS catalog (right scale). The blue-shaded bars on top indicate the uplift periods between 1950-52, 1969-72, 1982-84, and since 2005. The yellow bar refers to the occurrence times of the approximately 2,600 detected earthquakes without associated magnitudes . (c) Zoomed section of uplift and seismicity with $M_d \geq 0.45$ events recorded in the local catalog since 2005. The magnitudes are randomized in both panels within their bins for better visibility, and the vertical dashed lines mark the beginning of the earthquake recordings and the end of the analyzed dataset, respectively.

Aftershock sequences embedded in the observed seismicity. (a) Stacked seismicity relative to $M_d \geq 3$ earthquakes occurred since 2005 at Campi Flegrei. Points refer to the event magnitudes (left scale) as a function of the occurrence times relative to the corresponding $M_d \geq 3$ events. The curves (right scale) refer to the average foreshock (blue) and aftershock (red) rate of the $M_d > 0.45$ events per mainshock. The left inset shows an example of one of the stacked sequences (green points, same scales). The right inset shows the stacked rates as a function of the absolute time in a double logarithmic plot, indicating an Omori-type decay with $p \approx 0.5$. (b) The points show the average excess of aftershocks over foreshocks, i.e. the average difference between the number of events N_2 in the following half-day and the

number N_1 in the preceding half-day, as a function of the cutoff magnitude for the target events. The crosses refer to the same analysis for selecting the events in non-overlapping magnitude bins [1, 2), [2, 3), [3, 4), and [4, 5). The observations show an exponential increase (dotted line) of the excess value with mainshock magnitude, as expected for aftershock triggering. In contrast, no increase is seen in the inset panel, showing the corresponding results for sequences consisting of the original occurrence times but with randomized magnitudes, where points refer to the mean and bars to plus and minus one standard deviation for 100 randomized sequences.

Consistency between modeled and observed seismicity. (a, b) Observed monthly rates of $M_d > 0.45$ events (gray) compared to the RS (blue) and the hybrid ETAS (brown) model fits with parameters given in Table 1. Panel (b) shows the same as panel (a) but for a logarithmic y-axis. The inset in (a) shows the corresponding cumulative numbers of predicted and observed events. The 95% confidence intervals, referring to Poisson distributed errors, are marked in (b) by the dashed lines (RS) and shaded area (ETAS). The percentages of the observations falling outside the confidence intervals are provided in the legend. Crosses on the bottom axis in (b) refer to months without recorded events. (c) The outcome of 10^4 Monte-Carlo simulations of the hybrid ETAS model for 1905-2025 with parameters fixed by the fit of the $M_d > 0.45$ events for $t > 2005$, compared with the $M_d \geq 3$ events recorded in the HORUS catalog. Here, the mean model rates are rescaled to give the observed number of $M_w \geq 3$ since 1980. The blue bars at the top indicate the uplift phases and the vertical dashed lines correspond to the onset times according to the Kaiser effect.

Pseudo-prospective forecasts. Observations (points) and median forecasts (curves) of (a) the number of $M_d \geq 0.45$ events and (c) their maximum magnitude in the next week. Panels (b) and (d) show the corresponding results for one-month forecasts. Shaded areas represent the 68%, 90%, and 95% confidence intervals of the forecasts. The step size between forecasts is one week.

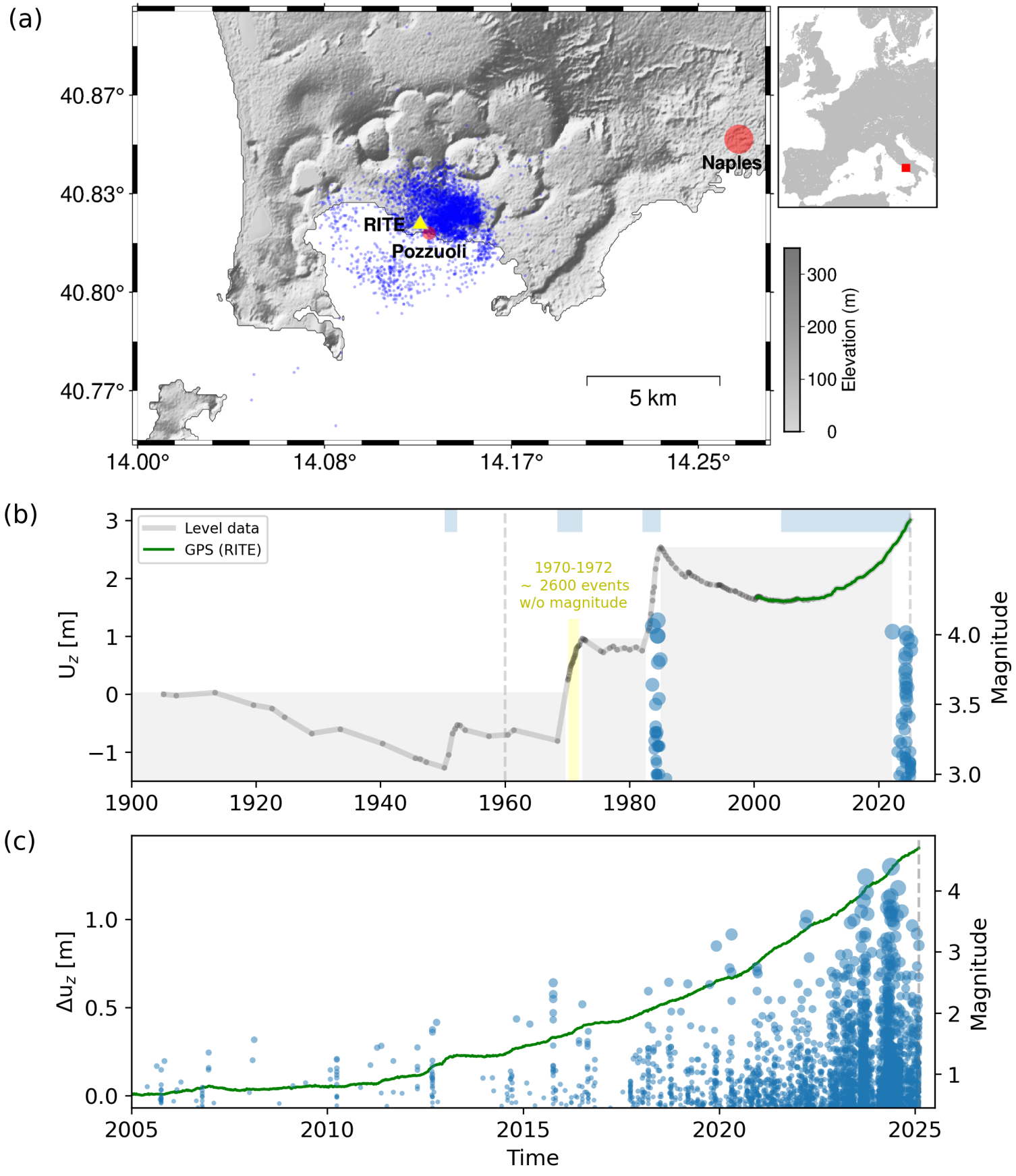
(a)
40.87°
40.83°
40.80°
40.77°
14.00°
14.08°
14.17°
14.25°
RITE
Pozzuoli
Naples
5 km
300
200
100
0
Elevation (m)
(b)
Level data
GPS (RITE)
1970-1972
~ 2600 events
w/o magnitude
U_z [m]
Magnitude
1900
1920
1940
1960
1980
2000
2020
(c)
Δu_z [m]
Magnitude
2005
2010
2015
2020
2025
Time

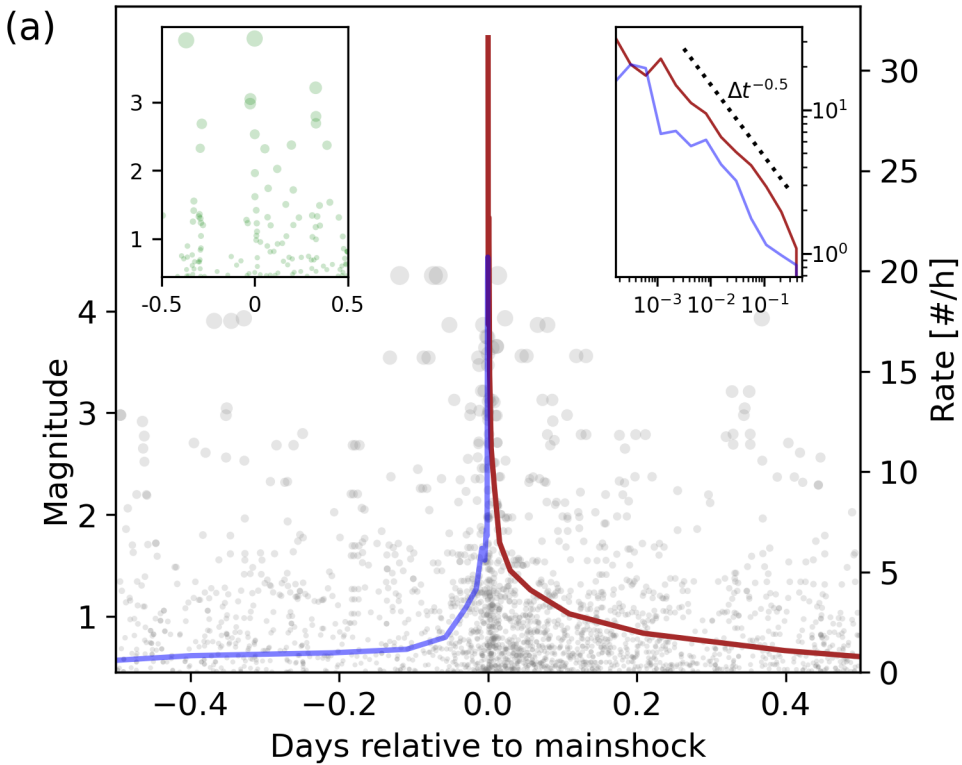
(a)
Magnitude
Rate [#/h]
Days relative to mainshock
$\Delta t^{-0.5}$

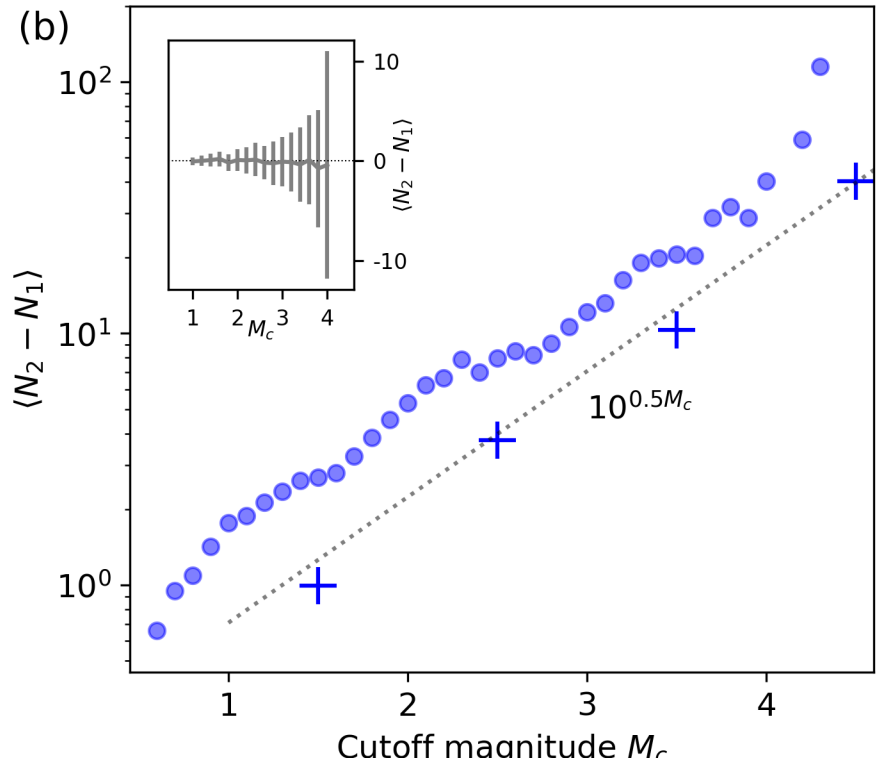
(b)
$\langle N_2 - N_1 \rangle$
Cutoff magnitude M_c
$10^{0.5M_c}$
$\langle N_2 - N_1 \rangle$
M_c

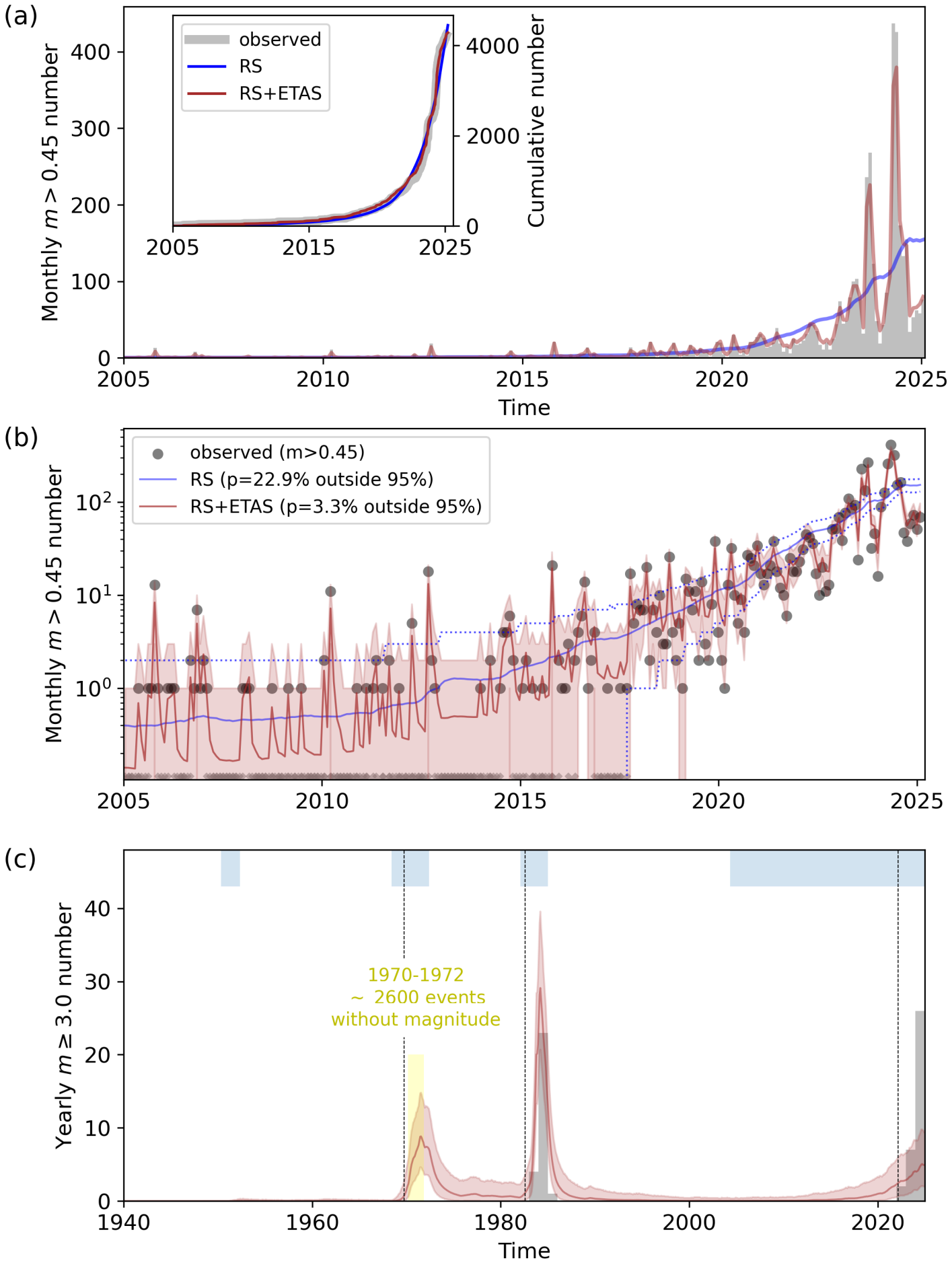
(a)
observed
RS
RS+ETAS
Monthly $m > 0.45$ number
Cumulative number
Time
(b)
observed (m>0.45)
RS (p=22.9% outside 95%)
RS+ETAS (p=3.3% outside 95%)
Monthly $m > 0.45$ number
(c)
1970-1972
~ 2600 events
without magnitude
Yearly $m \geq 3.0$ number
Time

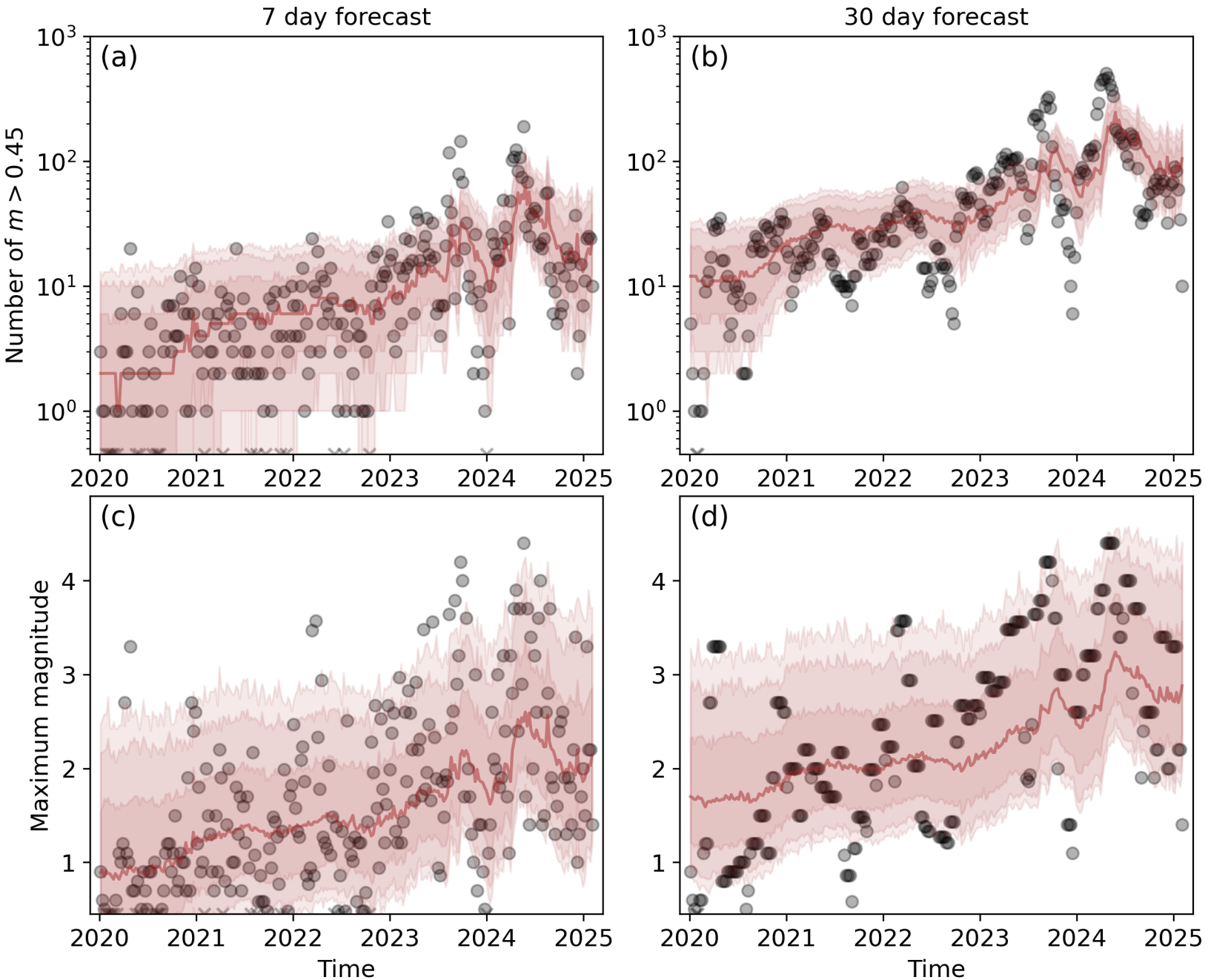
7 day forecast
30 day forecast
(a)
(b)
(c)
(d)
Number of $m > 0.45$
Maximum magnitude
Time
Time
10^0
10^1
10^2
10^3
1
2
3
4
2020
2021
2022
2023
2024
2025